A Modeling Study of Acoustic Propagation Through Moving Shallow-Water Solitary Wave Packets

Timothy F. Duda and James C. Preisig, *Member, IEEE*

***Abstract*— Propagation of 400-Hz sound through continental-shelf internal solitary wave packets is shown by numerical simulation to be strongly influenced by coupling of normal modes. Coupling in a packet is controlled by the mode coefficients at the point where sound enters the packet, the dimensions of the waves and packet, and the ambient depth structures of temperature and salinity. In the case of a moving packet, changes of phases of the incident modes with respect to each other dominate over the other factors, altering the coupling over time and thus inducing signal fluctuations. The phasing within a moving packet varies with time scales of minutes, causing coupling and signal fluctuations with comparable time scales. The directionality of energy flux between high-order acoustic modes and (less attenuated) low-order modes determines a gain factor for long-range propagation. A significant finding is that energy flux toward low-order modes through the effect of a packet near a source favoring high-order modes will give net amplification at distant ranges. Conversely, a packet far from a source sends energy into otherwise quiet higher modes. The intermittency of the coupling and of high-mode attenuation via bottom interaction means that signal energy fluctuations and modal diversity fluctuations at a distant receiver are complementary, with energy fluctuations suggesting a source-region packet and mode fluctuations suggesting a receiver-region packet. Simulations entailing 33-km propagation are used in the analyses, imitating the SWARM experiment geometry, allowing comparison with observations.**

***Index Terms*— Coupled mode analysis, underwater acoustic propagation, underwater acoustics.**

I. Introduction

MANY observational studies have shown high-amplitude nonlinear internal waves to be common on continental shelves and in shallow seas [1], [2]. They are most prevalent during the warm seasons of strongest stratification. These waves have strong effects on the coastal acoustic waveguide, and it is important to consider the possibility that they influence acoustical signals in the coastal ocean. For example, a number of modeling studies indicate that these waves can cause erratic exchanges of acoustic energy between normal modes at frequencies of a few hundred hertz, which in turn may cause strong signal fluctuations in coastal seas [3]–[5].

The strength of internal-wave effects on acoustics motivated a detailed study of the mode-coupling behavior of individual solitary waves [6]. That study considered 200- and 400-Hz sound in a waveguide of 50-m depth. It was shown that energy will shift between normal modes at the steep faces of internal solitary waves. This coupling occurs over propagation ranges of tens of meters, small in comparison to the so-called mode cycle distance, defined as the scale of the wavenumber difference of the pair of interacting modes. For wave horizontal scale L less than about 200 m, the coupling at each face is well approximated by a sharp interface approximation, meaning that the effect of the entire wave can be approximated well by coupling at a pair of interfaces separated by approximately L (a square well). This numerical work was done concurrently with the SWARM propagation experiment east of New Jersey [7]–[9]. SWARM signals showed strong variability at time scales of minutes to hours, which we briefly show here for comparison with our model results.

One of the insights made possible by the sharp interface approximation [6] is that the relative phases (differences of phases of the complex mode-amplitude coefficients) of the dominant modes at the interfaces are the most significant factor in determining the coupling. Since solitary waves generally appear in packets rather than individually [10]–[12], this paper extends the analysis to packets of waves. Earlier studies have investigated packet effects by attempting to relate the physical characteristics of packets to the coupling [3], [4]. However, it is shown here that very different coupling will result from the same packet shifted a few hundred meters, with all other parameters unchanged, consistent with packet propagation. Relative phasing between dominant modes plays a pivotal role in controlling the fluctuations caused by an entire packet, as it does with individual waves [6], despite the added complexity of the problem.

The study is made using numerical solution of the parabolic wave equation (PE) and a more efficient approximate coupled-mode propagation technique. As in our earlier work [6], we consider idealized wave shapes, which simplify the problem yet still divulge the basic physics. Our most restrictive idealization is not allowing the moving packets to change their shape as they propagate tens of kilometers, a simplification of naturally evolving solitary wave packets [2], [11], [12]. This is done to isolate and study the effects due solely to packet motion, excluding effects of packet evolution.

We have two basic results.

1) Solitary wave packets can cause gain or loss of acoustic energy received at ranges of order 35 km through the interplay of packet-induced mode coupling and bottom-induced attenuation of higher modes. The net gain is dependent on packet position and source depth.
2) Superimposed on those persistent signal gains (or losses) are fluctuations having time scales of minutes.

Manuscript received May 21, 1998; revised November 9, 1998. This work was supported by the Office of Naval Research under Grant N00014-95-1-0029 and Grant N00014-95-1-0051. This is WHOI contribution number 9826.

The authors are with the Applied Ocean Physics and Engineering Department, Woods Hole Oceanographic Institution, Woods Hole, MA 02543 USA.

Publisher Item Identifier S 0364-9059(99)01069-9.

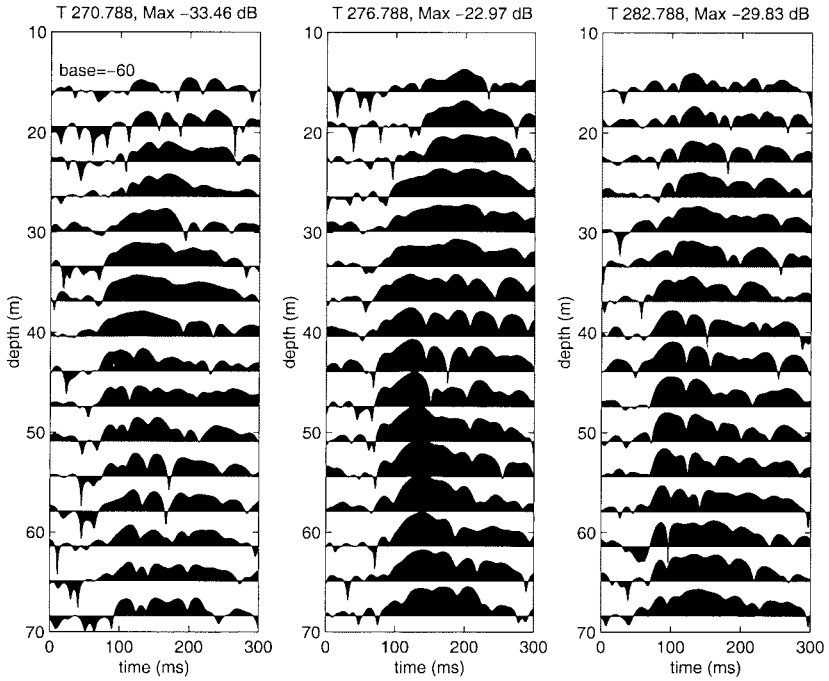

Fig. 1. Example SWARM pulses at 6-min intervals are shown. These are from three consecutive groups of 22 pulses; the fifth pulse (sequence) of each group is shown. The start times are indicated above, in minutes from the beginning of day 213, 1995. The intensity baselines are at -60 dB, the spacing between curves (phones) is 3.5 m, and the intensity scale is 10 dB per m of indicated depth.

The paper is organized as follows. Example signal fluctuations from the 1995 SWARM coastal acoustic experiment are shown in Section II. The simulation procedures are described in Section III. Section IV shows signal strength fluctuations from a benchmark calculation through a moving packet; the magnitude of the packet effect is compared with the effect of lower amplitude stochastic thermocline displacements, the so-called background. Section V shows how signal strength fluctuations from moving packets depend on interference between specific couplings for the packet as a whole. Section VI shows the patterns of mode coupling and excitation within packets and the sensitivity to intermodal phase. Section VII shows temporal coherence of acoustic fields through moving packets. Section VIII shows that packets act to smooth modal energy content in our simulations. A summary concludes the paper.

II. Signal Variability in the SWARM Experiment

One component of the SWARM experiment [7]–[9] was the transmission of 400-Hz pulses to a moored vertical line array at range 33 km offshore of the source. The source was at a depth of 29 m at a site 54 m deep. The array was in 70.5 m of water. The array had 16 hydrophones at 3.5-m spacing from 14.9 to 67.5 m depth. The pulses had about 100-Hz bandwidth and were synthesized using phase encoded 5.11-s 511-digit M Sequences [13]. The digit length was four cycles. Transmissions were repeated at 6-min intervals, with each transmission consisting of 23 sequences lasting 117.53 s.

The receptions indicate acoustic scattering by the intervening medium in the sense that many arrivals of each of the dominant acoustic modes were observed rather than only one. The timing fluctuation behavior of the mode arrivals has been analyzed [9]. Intensity fluctuations have not been analyzed in detail, but some aspects of the intensity fluctuations are shown here to qualitatively illustrate the behavior.

Fig. 1 shows a pulse from each of three consecutive transmissions. The pulses vary strongly in character at time scales greater than a few minutes. Note that the maximum amplitude differs by more than 10 dB between the first and second transmissions.

To distill the observations down to a simple estimate of received energy, the broad-band pulse signals can be incoherently averaged. The chosen quantity is the depth-averaged and time-averaged square of the matched-filter version of the sound pressure levels of the 16 phones for the duration of a pulse, $E = \sum_z \sum_t p^2$. E would not fluctuate if the source and receiver were fixed in a nonfluctuating ocean.

Fig. 2 shows the log-energy $I = 10 \log_{10}(|E|/\overline{E})$ during a 14-h section of the SWARM experiment, where the overline indicates an average over the 14 h. An expanded view of a shorter time interval is also shown. This fluctuation in the depth-averaged energy rules out the simple Doppler shifting of a mode interference pattern at the receive array, caused by currents or equipment motion, as a trivial explanation of the fluctuations observed in Fig. 1. The peak-to-peak energy fluctuation is about 16 dB, and on a few occasions there is an approximately 7-dB fluctuation in I over a period of only several minutes (e.g., minute 237). Large and rapid fluctuations occur both during periods of high mean E and low mean E. Simulation results in the remainder of this paper are intended to provide possible explanations of these observations.

III. Numerical Modeling

The two methods used to generate simulated acoustic fields are described here. Cylindrical geometry is used throughout,

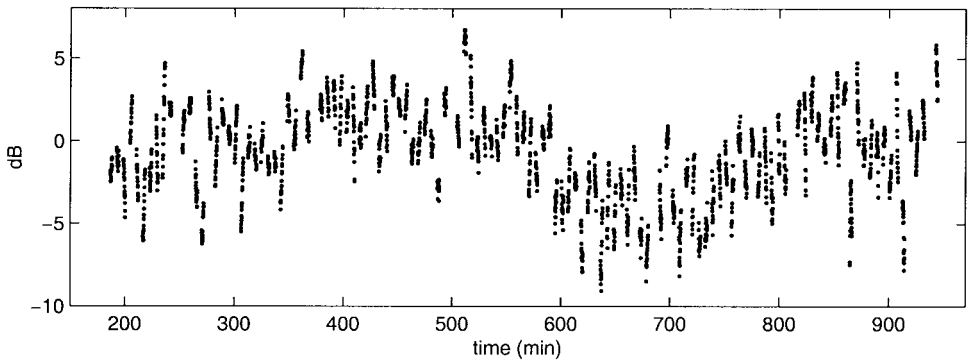

(a)

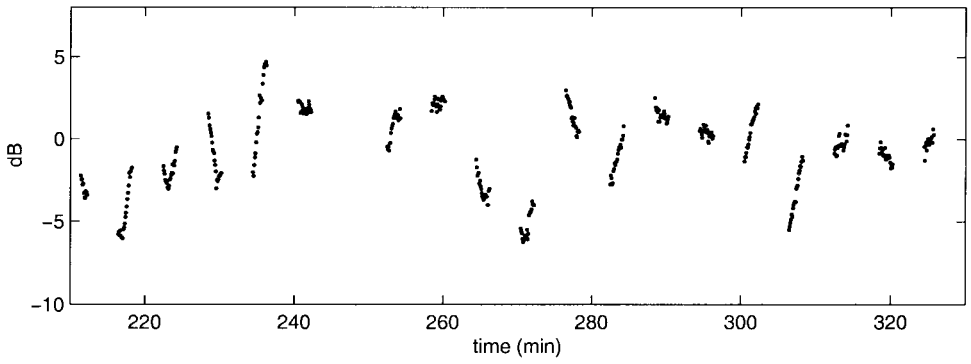

(b)

Fig. 2. Depth-averaged log-intensity time series $I(t)$ from the SWARM experiment. The indicated times are minutes from the beginning of day 213.

with the acoustic source at variable depth positioned at $r = 0$. The outgoing radiation condition is satisfied at infinite r, so that field characteristics at ranges lesser or greater than some benchmark position (such as packet location) are sometimes referred to as "before" and "after" the benchmark, respectively.

A. Parabolic Equation Solution

The finite element PE (FEPE) high-angle approximation code [14], [15] is used to solve the parabolic equation in two-dimensional (2-D) vertical slices. The code was modified to provide the complex acoustic pressure field as an output. The numerical domain is 33 km in the horizontal and 200 m in depth. The water depth is 60 m. The background sound-speed structure $c(z)$ is similar to that of Preisig and Duda [6], with a surface layer of 15 m in depth and $c = 1522$ m/s, a bottom layer from 30 to 60 m of $c = 1494$ m/s, and a linear gradient layer between. Baroclinic mode-one internal waves are approximated with equal displacements of the two interfaces. The resulting sound-speed perturbation field is made simpler than that of multiple baroclinic mode simulations [16] to allow detailed analysis of the effects of mode-one waves. Fig. 3 shows displacements $\eta(x)$ for a three-soliton packet. This packet geometry is used for most of the results in this paper. The relationship of amplitude a and horizontal scale L of the soliton displacements $\eta(x, t) = a\,\mathrm{sech}^2[(x - ct)/L]$, which are solutions of the Korteweg de Vries (KdV) nonlinear wave equation [2], [17], are not restricted to the KdV solutions for this particular waveguide because the sound and the soliton may not be propagating in precisely the same direction. The position of the center of the right-hand wave is arbitrarily

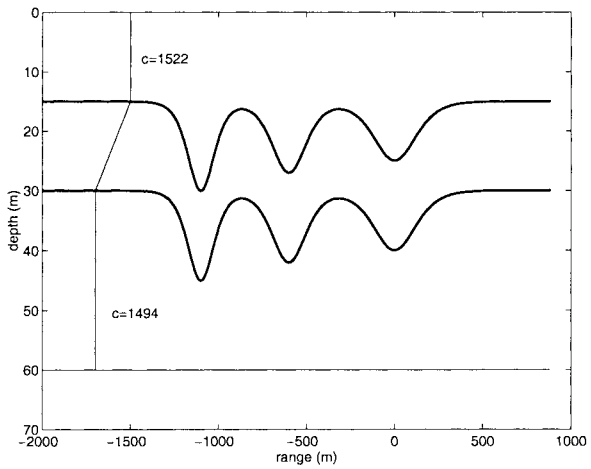

Fig. 3. Geometry of the wave packets used in the numerical simulations. Each wave is a sech-shaped downward displacement of the thermocline separating the isothermal layers. The packet shown is at $R_p = 0$.

chosen as the "position" of the packet, R_p. The bottom has $c = 1673.3$ m/s, density 2000 kg/m^3, and p-wave attenuation of 0.7 dB per wavelength. The range increment is 0.8 m and the depth increment is 0.25 m. The Pade expansion parameter NPADE is set to 2. The computed field is saved at 0.5-m depth increments and 8-m range increments.

B. Packet-Coupling Matrix

The PE must be solved numerically, repeatedly, for the entire domain of the moving packet if the field is desired for analysis. However, a simpler approximate method can be

used to compute distant received signals. The coupling due to a packet at $r = R_p$ can be described by a range-dependent matrix $\mathbf{C}$

$$\vec{M}^+ = \mathbf{C}(R_p)\vec{M}^- \tag{1}$$

where $\vec{M}^-$ and $\vec{M}^+$ are vectors of the complex mode amplitude coefficients before and after traversing the wave packet, respectively. If $\mathbf{C}$ is known, then the effects of moving packets can be computed using (1) at the packet and using adiabatic mode propagation elsewhere. Despite its range dependence, $\mathbf{C}$ can be computed from a set of PE computations within a domain slightly larger than the packet in the horizontal at arbitrary range from a source. The method is an approximation because it includes only propagating modes and disallows coupling to evanescent modes.

Under the assumption that the packet does not change shape, the dependence of $\mathbf{C}(R_p)$ on R_p is simply multiplication by a scaling factor. This is shown using the coupled mode equations for a range-dependent environment [18]. Let $M_j(r)$ denote the coefficient of propagating mode j at range r from the source, and define

$$P_j(r) = r^{1/2} M_j(r) \tag{2}$$

to be the mode coefficients with cylindrical spreading attenuation removed (the despread coefficients). The coupling equations can then be written

$$\frac{d^2 P_j(r)}{dr^2} + \left(k_j^2(r) + \frac{1}{4} r^{-2}\right) P_j(r) = -\sum_l D_{lj}(r) P_l - \sum_l B_{lj}(r) \frac{dP_l(r)}{dr}. \tag{3}$$

Here, $k_j(r)$ is the horizontal wavenumber of the jth mode at range r. $D_{lj}(r)$ and $B_{lj}(r)$ are parameters which depend only on the environment and its first and second derivatives with respect to r. The r^{-2} term can be neglected at sufficient distance from the source, so the second term on the left-hand side reduces to the familiar $k^2 P$ form. Under these assumptions, the coefficients P_j depend on r only through the dependence on r of the environmental characteristics. Thus, the approximate coupling matrix describing the effect of a packet on the coefficients P_j will be unchanged in the reference frame moving with the packet. The approximation can be written

$$\vec{P}^+ = \tilde{\mathbf{C}}\vec{P}^- \tag{4}$$

where $\tilde{\mathbf{C}}$ is invariant with range. Let the ranges of the start and end of a soliton packet at R_p be given by $(R_p - \delta R^-)$ and $(R_p + \delta R^+)$, respectively. Substitution of (2) into (4) and comparing with (1) yields

$$\mathbf{C}(R_p) = \left(\frac{R_p - \delta R^-}{R_p + \delta R^+}\right)^{1/2} \tilde{\mathbf{C}}. \tag{5}$$

Let the complex horizontal wavenumber of the jth mode in the range-independent (background) environment outside of the packet be given by $k_j = kr_j + i\alpha_j$ where $i = (-1)^{1/2}$ and kr_j and α_j are real numbers greater than or equal to zero. Let $\vec{M}(0)$ be mode coefficients as excited by the source at range $r = 0$. Using the far-field expansion for the Hankel function and setting $\delta R^- = \delta R^+ = \delta R$ for simplicity, the coefficients at ranges $R_r > R_p + \delta R$ can be written

$$\vec{M}(R_p, R_r) = \left(\frac{R_p + \delta R}{2\pi R_r}\right)^{1/2} \mathbf{\Lambda}(R_r - R_p - \delta R)\mathbf{C}(R_p) \cdot \left(\frac{1}{R_p - \delta R}\right)^{1/2} \mathbf{\Lambda}(R_p - \delta R)\mathbf{K}^{-(1/2)}\vec{M}(0). \tag{6}$$

Here, $\mathbf{K}$ and $\mathbf{\Lambda}(r)$ are diagonal matrices with $K_{jj} = k_j$ and $\Lambda_{jj}(r) = e^{ik_j r} = e^{ikr_j r} e^{-\alpha_j r}$. Substituting (5) into (6) and canceling the spreading factors yields

$$\vec{M}(R_p, R_r) = (2\pi R_r)^{-(1/2)} \mathbf{\Lambda}(R_r - R_p - \delta R) \cdot \tilde{\mathbf{C}}\mathbf{\Lambda}(R_p - \delta R)\mathbf{K}^{-(1/2)}\vec{M}(0). \tag{7}$$

Using the calculated modal coefficients, the acoustic field at range R_r is given by

$$p(R_p, R_r, z) = \sum_j M_j(R_p, R_r)\Psi_j(z) \tag{8}$$

where $\Psi_j(z)$ is the jth mode function. For numerical implementation, $\mathbf{C}$ is found by transmitting modes into a packet one at a time with FEPE.

Fig. 4 shows the acoustic field intensity at range $R_r = 33$ km, as a function of soliton packet (Fig. 3) position, calculated using FEPE. The environmental parameters used are those described in Section III-A, and the source depth is 18 m. Fig. 4 (center) also shows the comparable intensity for the same conditions computed using the coupling matrix expressions (7) and (8). Finally, the difference between these intensity fields is shown (the difference of the decibel values, equivalent to the ratio of the intensities). The comparison is close a large fraction of the time and spatial patterns are similar, confirming the validity of using (7) and (8) to model the effect of the packet. Fig. 5 shows the depth-averaged acoustic intensity within the water column at the receiver E_m as a function of R_p calculated for identical conditions using each of the methods. The methods generally agree well. E_m is a monochromatic (or model) version of E used in Section II.

IV. Example Packet-Coupling Effects

Using the idealized situation of a three-soliton packet propagating unchanged over the 33-km receiver-to-source distance, we analyze E_m as a function of R_p. The behavior over short intervals of R_p should be reliable despite the absence of packet and wave dispersion. Fig. 3 shows the model packet, which moves to the left (R_p decreasing), with the leading soliton 1100 m ahead of the third soliton. Note that the leading soliton in a group is the tallest and the narrowest for KdV solutions and in some (but not all) observations. Away from the packet, the domain is described by the background sound-speed structure.

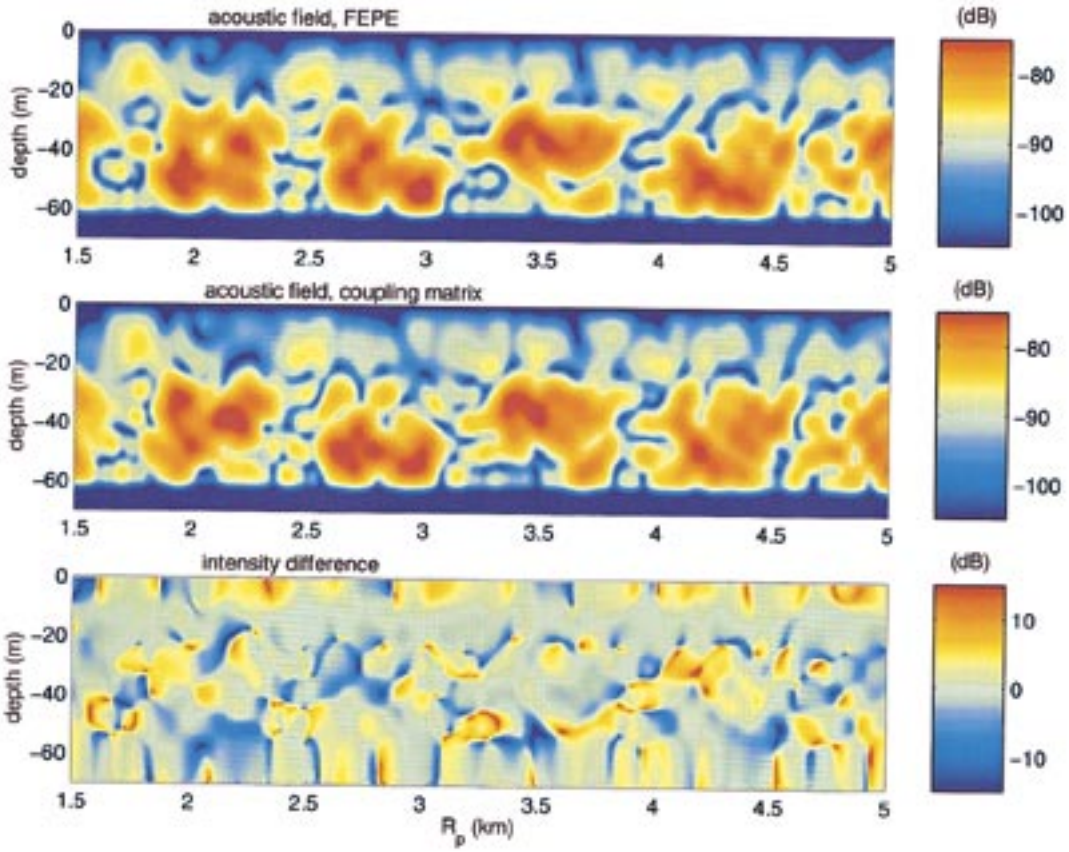

Fig. 4. Comparison of acoustic fields calculated using FEPE and mode-coupling matrix equations. Upper panel: Acoustic field strength in the water column at 33-km range for various R_p computed with FEPE. Middle panel: The same result as in the upper panel, computed using the coupling matrix technique. Lower panel: The difference of the fields in the other panels.

A. Example Packet Effect: Gain from Near-Source Waves

Fig. 6 shows the acoustic intensity at receiver position $R_r = 33$ km as a function of packet position, with source at 18-m depth and at $R_s = 0$. The packet moves from receiver to source as in SWARM. If the packet is assumed to move at a speed of 0.8 m/s, the 35-km R_p domain would correspond to 12.2 h, approximately one semidiurnal tidal period. Fig. 7 shows intensity at two depths. At 15 m, the packet produces fluctuations of about 15 dB of near-zero mean. At 40 m, where mode 1 energy is important, there are fluctuations of order 20 dB, but there is an additional gain of 20 dB when the packet is near the source which tapers to a few decibels for packet position near the receiver.

A striking result is significant signal gain or loss at the receiver, caused by the presence of the packet. This gain is related to the modal excitation pattern of the source which is discussed in Section VIII. If high-mode energy is excited and is then coupled into the least-attenuated first mode by a packet, then signal gain results. The highest gain of over 10 dB in depth-average intensity E_m occurs for R_p within a few kilometers of the source.

Fig. 8 shows E_m as a function of R_p. This measure of arrival energy at a receiver array is intended to be qualitatively comparable to the SWARM pulse energy observations (Fig. 2). The signal level is -90.7 dB with no solitons between the source and the receiver, i.e., with R_p less than -0.5 km or greater than 34.5 km. The signal level begins fluctuating as the packet passes over the receiver. The fluctuations increase in magnitude as the packet moves toward the source, with the local maxima following an approximately linear trend to a peak at -80 dB with the packet at the ranges of 1–2 km. The linear trend of maxima in decibels indicates an exponential curve with a range scale of about 15 km, or

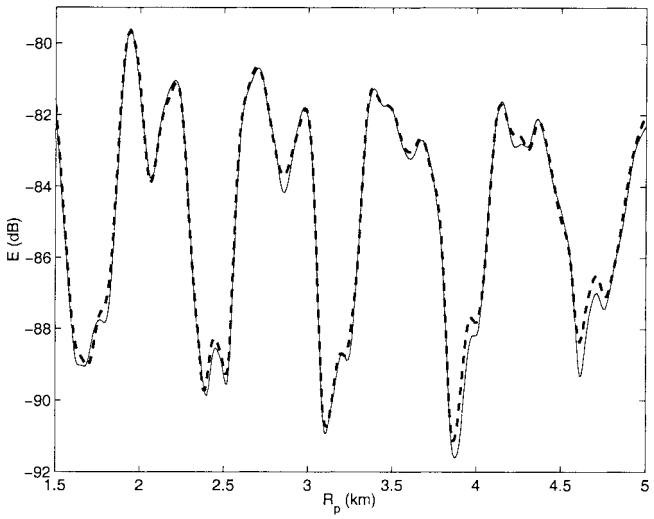

Fig. 5. Comparison of depth-averaged energy in acoustic fields calculated using FEPE (solid line) and mode-coupling matrix equations (dashed line).

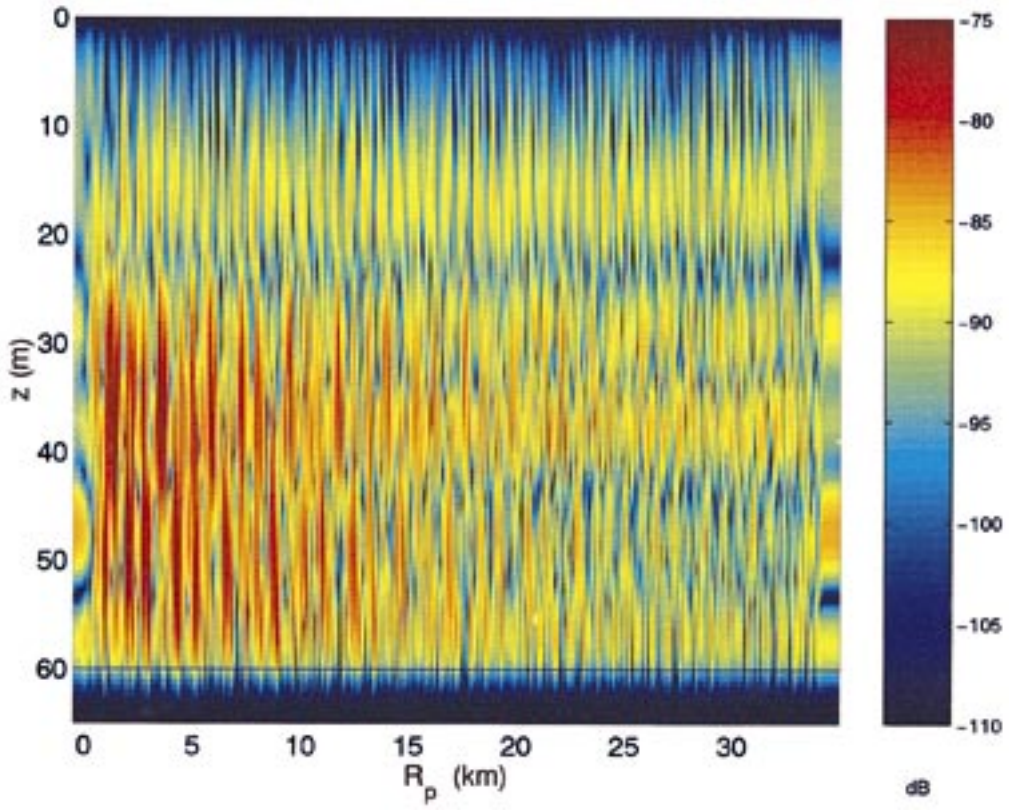

Fig. 6. Intensity at range 33 km as a function of depth and packet position R_p for a source at 18-m depth. $R_p = 0$ indicates packet at the acoustic source, $R_p = 33$ indicates packet at the receiver. This is simulation A.

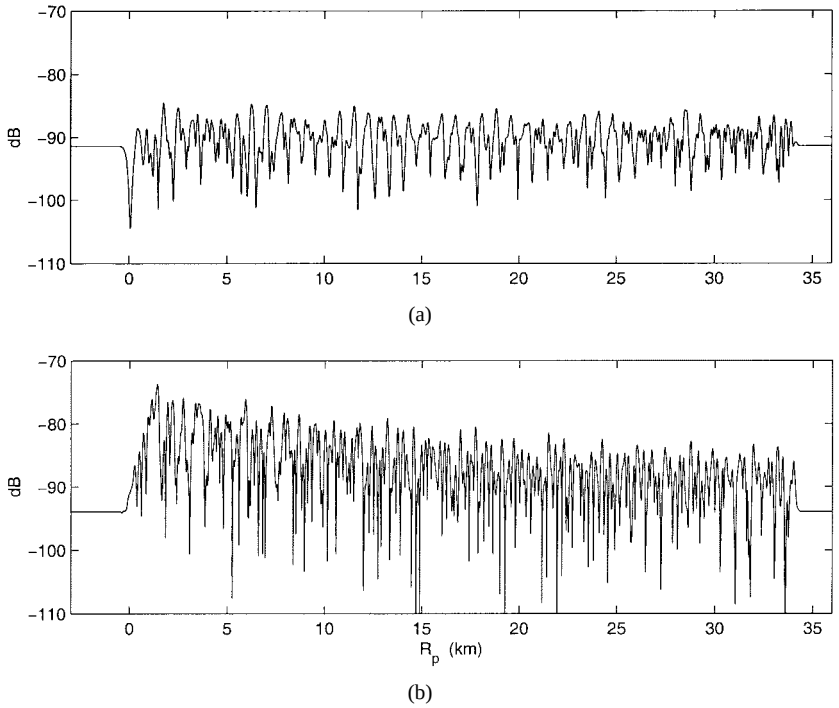

Fig. 7. Intensity as a function of packet position for two depths, (a) 15 and (b) 40 m. These are slices taken from the intensities shown in Fig. 6.

$\max(E_m) = E_{mr} \exp((R_p - R_r)/15\,000)$, where E_{mr} is the value of E_m at the receiver range R_r. The range of fluctuations grows with the maxima as R_p approaches R_s, with local minima remaining within a few decibels of the no-soliton E_m.

Fig. 9 is an expansion of a section of the Fig. 8 pattern. The order 10-dB energy fluctuations occur quasi-periodically, with a cycle distance of roughly 800 m. Details of the acoustic field in the vicinity of the packet are shown in the following

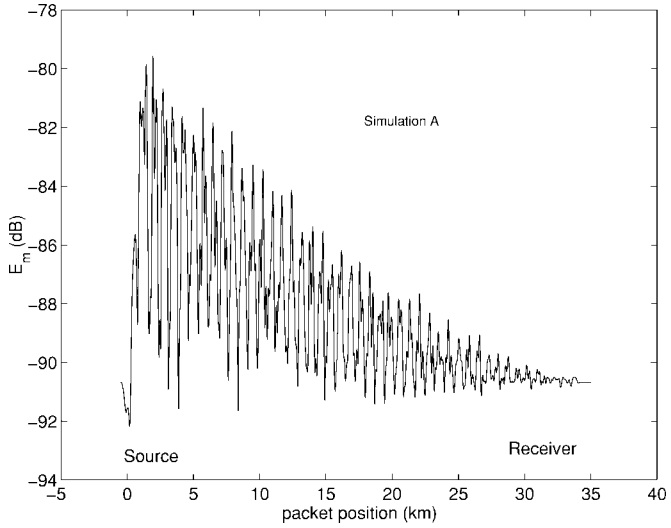

Fig. 8. Depth-averaged energy at the receiver as a function of packet position R_p for simulation A (see Figs. 6 and 7).

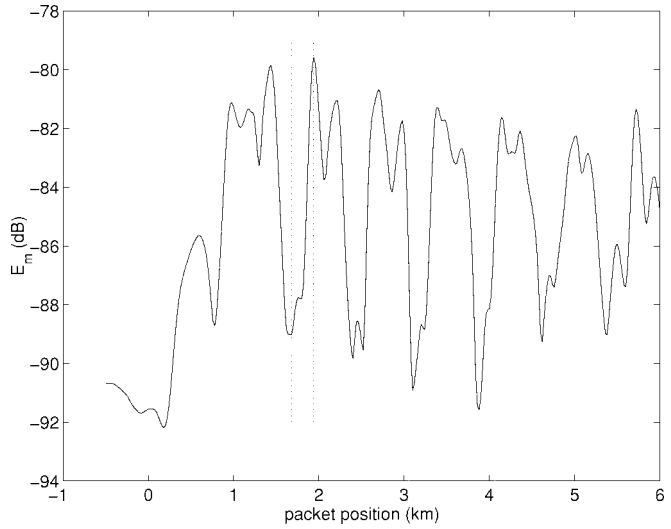

Fig. 9. Expansion of E_m of Fig. 8 (simulation A).

section for two packet positions marked in Fig. 9: $R_p = 1678$ m with weak received energy, and $R_p = 1938$ m with strong received energy. Fig. 10 shows a detailed view of a portion of the acoustic field of Fig. 6; Figs. 9 and 10 have the same R_p range.

B. Comparison of Packet and Background Effects

The packet influence on acoustics can be significantly stronger than that of ubiquitous thermocline fluctuations. The mode coupling from individual solitary waves has been shown to scale with wave amplitude [6] and this is expected to also be true for packets. To test this, the analysis was repeated with the same packet geometry but with reduced amplitudes (simulation B). The amplitudes were reduced to 10/4, 12/4, and 15/4 m, one-quarter of their previous values. Fig. 11 shows the modulation of the arriving energy E_m as a function of R_p. Comparing with Fig. 8, the overall behavior is close to being a scaled version of what happens with the larger packet, with only a slight 2-dB gain with the packet near the source, intermittent as before. There are more frequent occurrences of net loss relative to the packetless situation than for the previous run.

To compare the packet effect with that of background thermocline fluctuations, the variation with time is computed for sound propagating through a time-evolving quasi-random displacement field. The field and its variation are also computed for the scenario of a simulation-A type packet (10-, 12-, and 15-m wave amplitudes, Fig. 3) moving through the same time-evolving field.

As R_p is sequentially changed for a moving packet simulation, the quasi-random wavefield is computed from its one-dimensional Fourier transform at each step. *Ad hoc* procedures are used to give the quasi-random perturbations some resemblance to a slice through a 2-D wavefield, rather than actually computing a 2-D model of small continental-shelf internal waves, which would be conjectural in structure anyway. The wavefield is given temporal coherence by simultaneously adding constant *and* random phase perturbations to each spectral component from the previous step. The random perturbations are scaled with the wavelength, effectively reducing the dynamic range of phase velocities. The perturbation algorithm is $\theta_p = 0.008 S_n(k_x - k_c/2) + 1.8A(k_x/k_c)^{0.1}$ where θ_p is the phase perturbation, k_x is a Fourier set of horizontal wavenumbers, A is a uniform random variable within $[-0.5, 0.5]$, there are n points in the wavefield at 1-m spacing, S_n is the sign function, and $k_c = \pi$ rad/m is the Nyquist wavenumber. The wave power spectral slope is $k_x^{-1.8}$ between the fundamental Fourier wavelength and approximately $\pi/5$ rad/m, zero elsewhere. The perturbation is computed only every fourth k_x and repeated (interleaved), giving some phase stability in wavenumber. The field resulting from inverse transformation has these properties: the rms thermocline displacement is 1.16 m, the rms slope is 0.02, the peak-to peak displacement was about 7.5 m, and the temporal covariance is as shown in Fig. 12. For comparison, the rms thermocline displacement in the first 15 km of the backscatter record from SWARM [7, Fig. 24] is 1.6 m, with an rms slope of 0.013, sampled roughly each 30 m.

Fig. 13 shows the fluctuating E_m for the quasi-random wavefield with no solitons (simulation D). Fig. 14 shows the variation of E_m with R_p for propagation through the random wavefield and the moving soliton packet (simulation C). Comparison with Fig. 8, for identical packet conditions but no background waves, shows that the background waves have a weaker effect on energy than the packet. The effect of the fluctuating thermocline is greater than the effect of a packet with reduced amplitudes (compare Figs. 11 and 13).

V. Input-Mode Interference Modulation of Modal Content

A. Observed Behavior

The signal strength fluctuations shown in Sections III and IV are among the signature acoustic effects of soliton packets. It is important to note that these simulated fluctuations occur

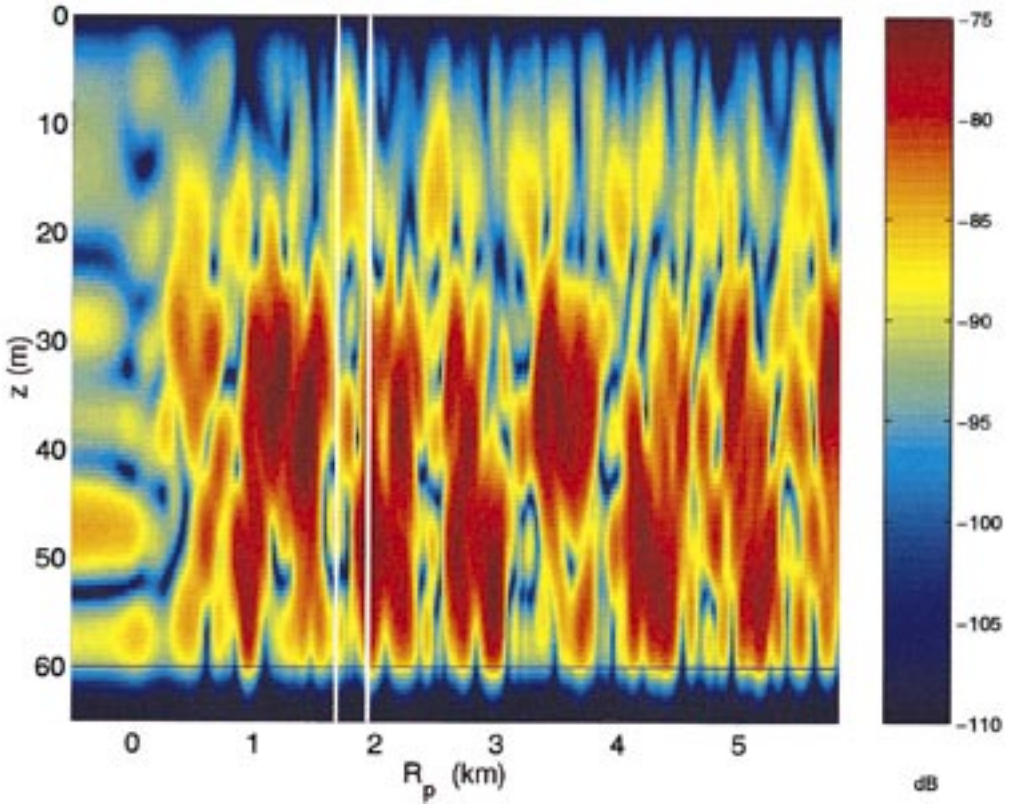

Fig. 10. Expansion of the acoustic energy data of Fig. 6. These data averaged over depth give the E_m of Fig. 9. A stripe shows the bottom interface at 60 m depth, and the vertical lines indicate results analyzed in detail in Section V.

as the packet moves but does not change shape. Returning to the results from simulation A with the source at 18-m depth (Figs. 9 and 10), when $R_p = 1678$ m the depth-averaged energy in the acoustic field at the receiver is approximately -89 dB. When $R_p = 1938$ m, the depth-averaged energy is approximately -80 dB. This abrupt change in the received energy level is caused by a change in mode coupling at the packet. The alteration of the relative phases of the modes governs the coupling and can be understood by examining the simulation output in detail.

Fig. 15 shows the modal content of the propagating acoustic field as a function of range with $R_p = 1678$ m. Fig. 16 shows the corresponding field with $R_p = 1938$ m. In both cases, energy in the acoustic field on the source side of the packet (before the packet) is concentrated in modes 3 and above, with little energy in modes 1 and 2. With $R_p = 1678$ m (Fig. 15), the energies in modes 2 and 3 on the receiver side of the packet (after) have been boosted a bit by the presence of the packet, but mode-1 energy remains small. With $R_p = 1938$ m, however (Fig. 16), the effect of the packet is to shift energy to modes 1 and 2. Because the lower order modes experience significantly less loss than the higher order modes as they propagate from the packet to the receiver, the altered coupling of energy into modes 1 and 2 accounts for the altered received energy.

When the packet transfers energy from the more strongly attenuated high-order modes into the low-order modes, the depth-averaged signal at a distant receiver will be strengthened. Conversely, when energy is taken from the low modes, the distant signal will be weakened. Signal strengthening is more likely to occur near a source where high modes are still energetic. Fig. 8 shows that gain occurs with the packet near a source of depth 18 m, but the gain is variable and does not always occur. In the remainder of this section, the effect of mode phasing on the spatial scale of the variability is analyzed. An approach is taken which treats the packet as

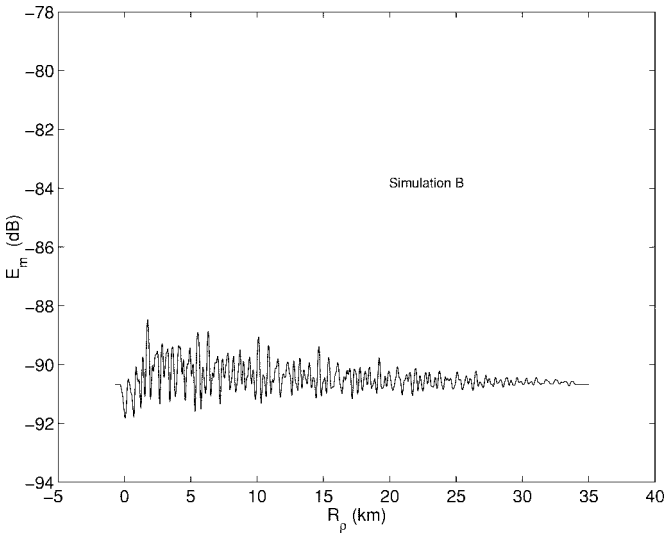

Fig. 11. Depth-averaged intensity for simulation B. All parameters are as in simulation A except for solitary wave amplitudes, which are reduced by a factor of 4 compared to A. The fluctuations are diminished with respect to simulation A (Fig. 8).

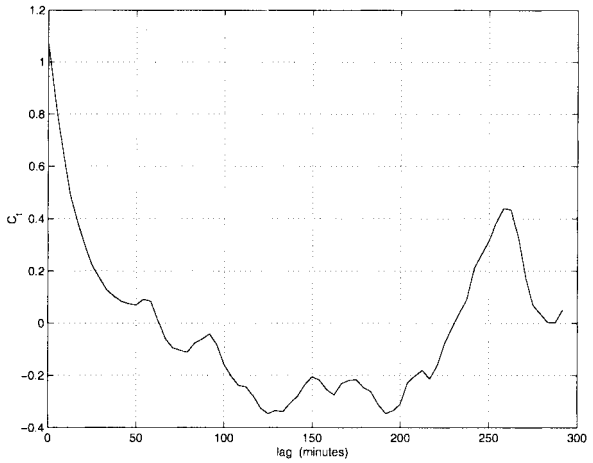

Fig. 12. Temporal covariance of the small quasi-random thermocline displacements of simulations C and D.

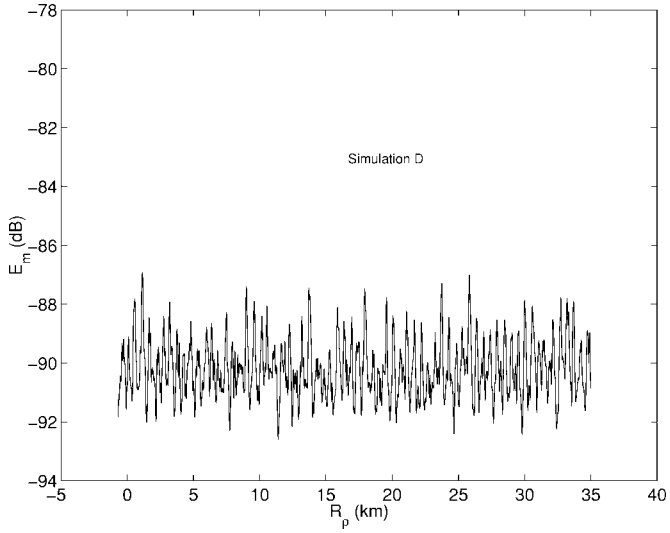

Fig. 13. Depth-averaged intensity for propagation through a field of time-varying small background waves. The waves have the temporal covariance of Fig. 12. For easy comparison with Fig. 8, the results are plotted versus position of a soliton packet moving at 0.8 m/s, although no soliton packet exists. This is simulation D.

a single coupling entity. The relation of soliton characteristics to the phase is discussed in Section VI.

B. Analysis

The mode-coupling matrix equations introduced in Section III provide a useful mechanism for analyzing this variability. Using (7), the energy in the jth received mode can be written

$$|M_j(R_p,R_r)| = \gamma_j(R_p,R_r) \cdot \left| \sum_l \tilde{C}_{jl} e^{ikr_l(R_p-\delta R)} e^{-\alpha_l(R_p-\delta R)} k_l^{-(1/2)} M_l(0) \right| \quad (9)$$

where $\gamma_j(R_p, R_r) = (2\pi R_r)^{-(1/2)} e^{-\alpha_j(R_r-R_p-\delta R)}$. The contribution of the lth incident mode to the sum in (9) is

$$E_{jl}(R_p) = e^{ikr_l(R_p-\delta R)} \tilde{C}_{jl} e^{-\alpha_l(R_p-\delta R)} k_l^{-(1/2)} M_l(0).$$

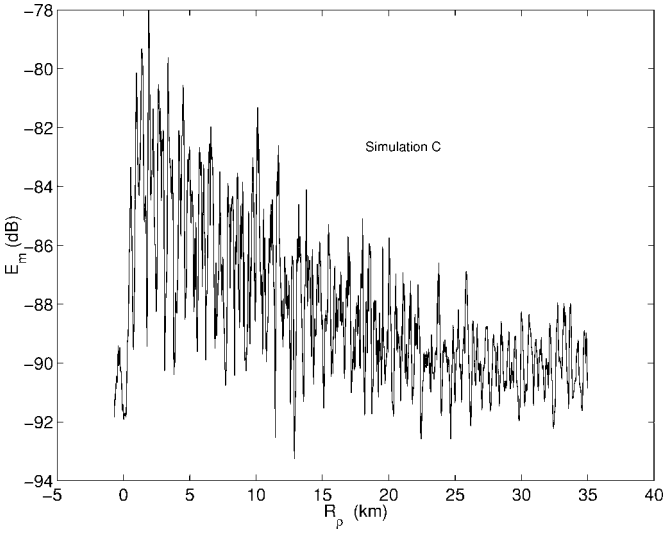

Fig. 14. Depth-averaged intensity for a simulation using a packet moving through the time-varying field of background waves. The packet is identical to that used to produce Fig. 8, and the background is as used in Fig. 13. This is simulation C.

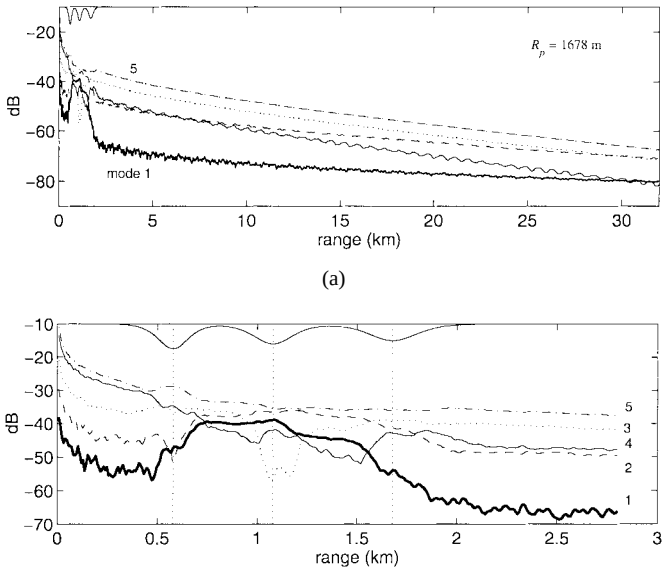

Fig. 15. (a) Magnitudes of mode coefficients 1–5 are shown for $R_p = 1678$ m. Results throughout the source–receiver domain are shown. The thermocline displacement geometry of the packet is plotted with arbitrary vertical scale at the top of the panel. The received energy is relatively weak with the packet at this location (1678 m), near the level it would have in the absence of the packet. (b) The data of the upper panel are plotted with an expanded scale, showing only the region near the packet and the source.

Letting $\beta_{jl}(R_p)$ denote the phase of $E_{jl}(R_p)$, this can be written

$$E_{jl}(R_p) = e^{i\beta_{jl}(R_p)} |\tilde{C}_{jl}| e^{-\alpha_l(R_p-\delta R)} k_l^{-(1/2)} |M_l(0)|.$$

For the environments under consideration in this paper, α values for the first six modes range from 1.2×10^{-5} to 8.5×10^{-5}, so their absorption loss is less than 0.08 dB over a range of 200 m. Clearly, the changes in the incident mode magnitudes over this distance do not account for the changes in the coupling behavior as packets move. This leaves the changes in the phase

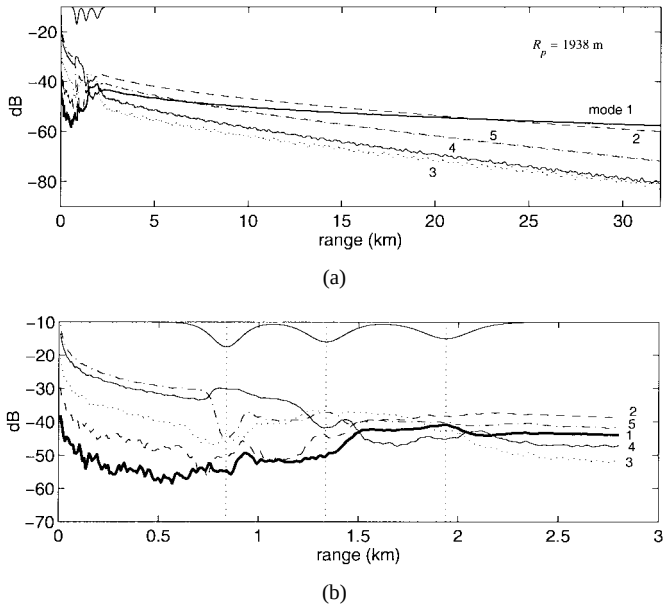

Fig. 16. (a) Magnitudes of mode coefficients 1–5 are shown as in Fig. 15, except for $R_p = 1938$ m. This R_p shows strong gain relative to the no-packet case. (b) The same curves are plotted with an expanded range scale for the area near the packet and the source.

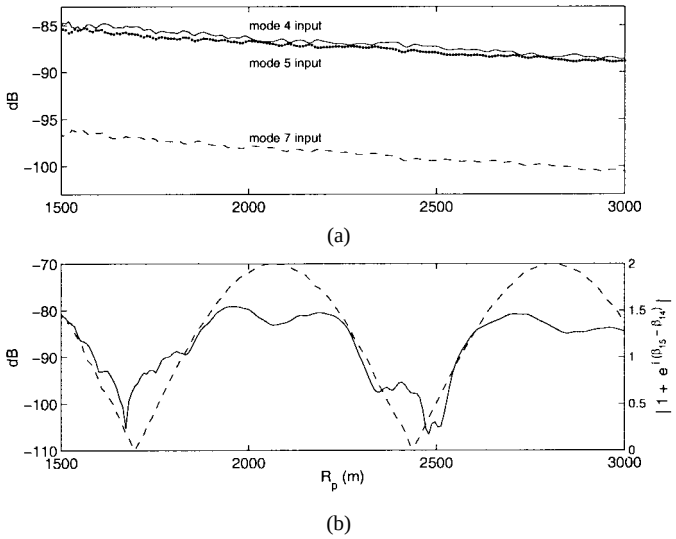

Fig. 17. (a) Magnitudes of inputs to mode 1 are shown, E_{1l}, with $l = 4$, 5, and 7, are shown. Curves for $l = 2$, 3, 6, and above 7 are below -105 dB. (b) The energy in mode 1 as it propagates out of the packet is shown (solid line). Also, the term $|1 + e^{i(\beta_{15}(R_p)-\beta_{14}(R_p))}|$ is shown (dashed line).

terms and their influence on the coherent sum in (9) as the factors governing changes over R_p of $M_j(R_p, R_r)$. The phase of each term of the coherent sum can be written as

$$\beta_{jl}(R_p) = \zeta_{jl} - \frac{\pi}{4} + kr_l(R_p - \delta R)$$

where ζ_{jl} equals the phase of $\tilde{C}_{jl}$. The phase of the incident mode (the final term) is the only range-dependent item and therefore causes the coupling changes with respect to R_p.

Consider the 18-m source-depth example simulation A. Fig. 17 shows $|E_{1j}(R_p)|$ for modes 4, 5, and 7. These are the three modes with the greatest amount of energy coupling into mode 1. Modes 4 and 5 dominate. Including only those two modes, the mode-1 coefficient at the end of the soliton packet can be expressed as

$$M_1(R_p, R_p + \delta R) \approx e^{-i(\pi/4)}(e^{i\zeta_{14}}\,|E_{14}(R_p)|\,e^{ikr_4(R_p-\delta R)} + e^{i\zeta_{15}}\,|E_{15}(R_p)|\,e^{ikr_5(R_p-\delta R)}) \quad (10)$$

which can be factored to yield

$$|M_1(R_p, R_p + \delta R)| \approx |E_{14}(R_p)|\left(1 + \left|\frac{E_{15}(R_p)}{E_{14}(R_p)}\right| e^{i(\beta_{15}(R_p)-\beta_{14}(R_p))}\right) \quad (11)$$

where $\beta_{15}(R_p) - \beta_{14}(R_p) = (\zeta_{15} - \zeta_{14}) + (kr_5 - kr_4)(R_p - \delta R)$. The phases of the modal inputs vary with a few meters wavelength for the 400-Hz case considered here, but the range-dependent factor which most significantly effects the changes in modal coupling on scales of several hundreds of meters is the difference $e^{i(kr_5-kr_4)(R_p-\delta R)}$. When $|E_{15}(R_p)/E_{14}(R_p)| \approx 1$, as is the case here, the phase-induced fluctuations in $|M_1(R_p, R_p+\delta R)|$ can be significant. Fig. 17(b) shows $|M_1(R_p, R_p + \delta R)|$. The quantity $|1 + e^{i(\beta_{15}(R_p)-\beta_{14}(R_p))}|$ is also plotted and follows the mode-1 output, showing that interference between modes 4 and 5 at the source side of the packet contributes to much of the mode-1 output variation. The period of the largest fluctuation is approximately 800 m, which corresponds closely to the interference distance for modes 4 and 5, $2\pi/(kr(4) - kr(5))$. This scale is much greater than the interference distances for modes 1 and 4 and modes 1 and 5.

For other output modes, similar relationships are observed between the horizontal scale of modal amplitude fluctuations at the receiver side of the packet and the modal interference distances of the input modes contributing most strongly to the output. *Coupling of energy into a mode by the packet is governed by beat patterns between the incident modes which couple significant energy into that mode.* The variability length-scale of a received mode is not directly predictable from the lengthscales of interactions between that mode and other modes. The amplitudes and scale lengths of each soliton in a packet, plus the mode shapes in the vertical, determine which modes are subject to coupling within a packet. This topic is the subject of previous work [6] and is touched upon in the next section, where mode-coupling behavior inside packets is shown for completeness.

Fig. 18(a) shows the modal content of the acoustic field at 33 km range as a function of packet position. The three modes shown (1, 2, and 5) control the output amplitude because at each position the other modes are much weaker than one or more of these. The modes fluctuate at different scales. Fig. 18(b) shows the sum of the energies of modes 1, 2, and 5 at 33-km range, which is very close to the depth-averaged energy for the acoustic field.

The role of mode phasing and attenuation in controlling the fluctuations in the received acoustic field gives insight into the dependence of these fluctuations on the environmental conditions for situations not shown here. Among the effects which can be predicted are the following.

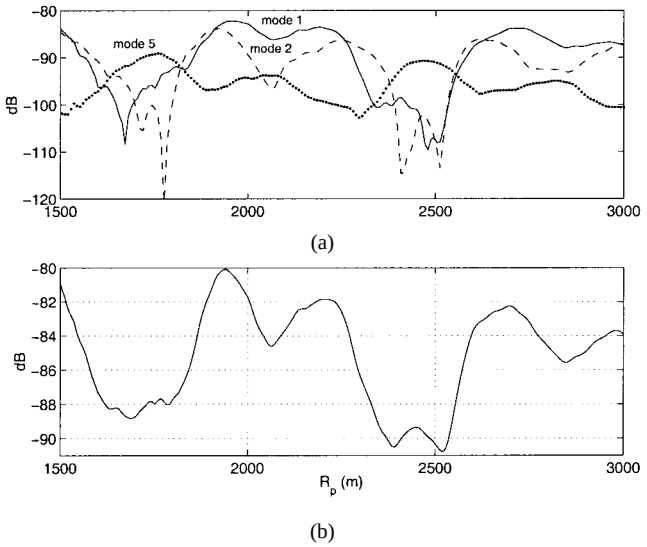

Fig. 18. (a) Energy content in modes 1–5 at the receiver is shown as a function of packet position. (b) The resultant energy in those modes.

1) If the incident acoustic field at a packet has one dominant mode, which can occur if the soliton packet is far from a source or if few modes are excited, then there will be no spatially rapid fluctuations in the packet-induced coupling and no rapid fluctuations in the received acoustic energy.
2) If the packet is close enough to the receiver so that the difference in the attenuation of the output modes occurring between the packet and the receiver is small, then the packet-induced energy fluctuations will be small.
3) If the end of the packet is close enough to the receiver so that significant energy remains in multiple modes at the receiver, then the spatial variability of the acoustic field at the receiver (i.e., at a selected depth) will fluctuate at time scales determined by modal interference patterns of the input and output modes.

VI. Coupling of Modes within Packets

The highly variable receptions at 33 km in our example (Figs. 8 and 9) have been shown to result from interference between discrete inputs of mode-4 and -5 energy into the efficiently propagating first mode. So much energy was coupled from modes 4 and 5 into mode 1 that constructive versus destructive interference of those inputs caused a 20-dB change in mode 1 at the receiver side of the packet.

Coupling within the individual solitons fluctuates wildly based on the modal phases at the source side of each soliton face. The relative modal phases are regular and predictable at the solitary wave face nearest the source, but because of coupling they are not predictable at the other wave faces without direct computation. Despite the complexity of the problem and the lack of intuitive tractability, the effects can be computed reliably and the dominant physics identified. The variability is governed by quasi-resonant interaction of two scales, those of mode interference and of individual solitons.

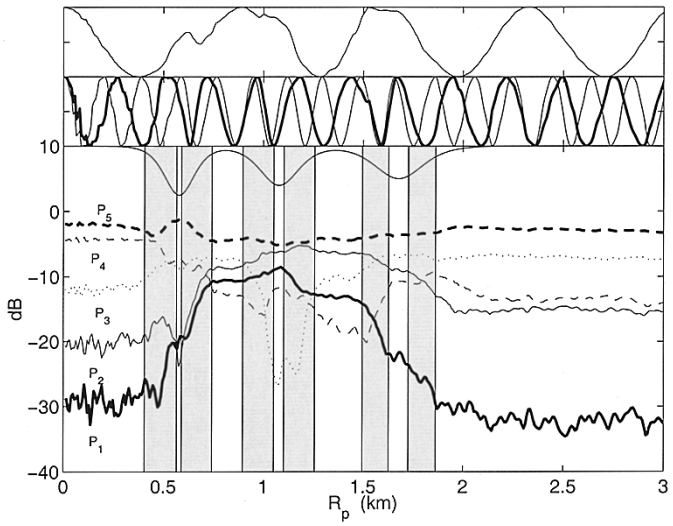

Fig. 19. (Lower panel) Normalized coefficients P are shown for modes 1–5 in the region of a packet at location $R_p = 1678$ m. The soliton shape is shown with arbitrary vertical scale at the top of the panel. Mode-coupling regions of steep thermocline slope are shaded. Coupling behavior is seen to differ at each soliton. (Middle panel) $\cos\theta_{41}^{-}$ (thick line) and $\cos\theta_{51}^{-}$ (thin line) are shown. Modes 4 and 5 were shown in Section V to provide input to mode 1 in the packet. The periodicity of the curves to the left and right of the packet contrasts with the strong phase variations in the packet. There is a tendency for modes 4 and 5 to couple when they are in phase rather than quadrature and dominate the energy, as in the left-hand wave. (Top panel) The phase function $\cos\theta_{45}^{-}$ is shown.

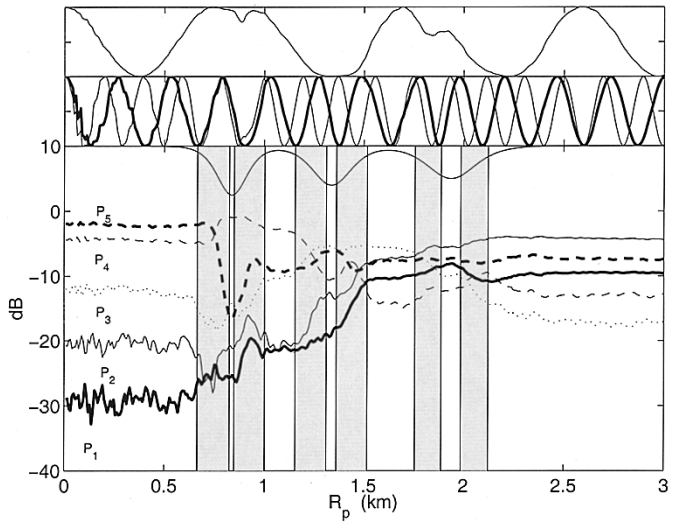

Fig. 20. (Lower panel) P as in Fig. 19, but with $R_p = 1808$ m. (Middle panel) $\cos\theta_{41}^{-}$ (thick line) and $\cos\theta_{51}^{-}$ (thin line) as in Fig. 19. (Upper panel) $\cos\theta_{45}^{-}$.

Figs. 19–21 show the normalized mode magnitudes P for three ranges $R_p = 1678$, 1808, and 1938 m and source depth 18 m. Two of these figures recapitulate the results of Figs. 15 and 16. The behavior of the modes throughout the packet is seen to fluctuate wildly and differ for the three cases. Mode phasing explains the seemingly random behavior of the coupling within the soliton packets, just as it explains the net coupling induced by the total soliton packet (previous section).

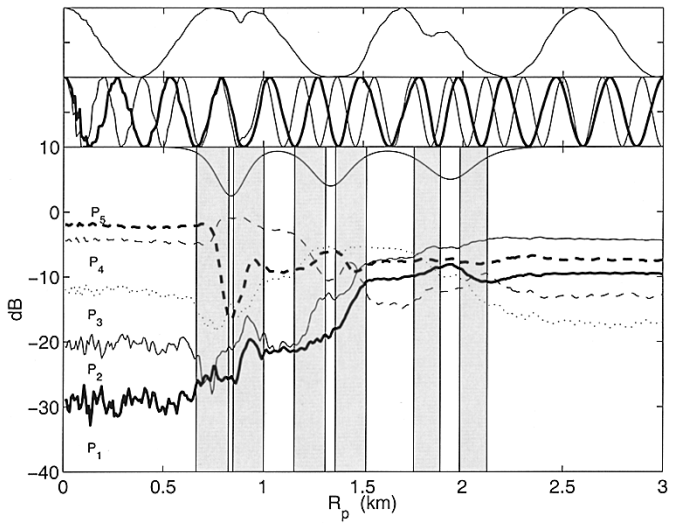

Fig. 21. (Lower panel) P as in Fig. 19, but with $R_p = 1938$ m. (Middle panel) $\cos\,\theta^-_{41}$ (thick line) and $\cos\,\theta^-_{51}$ (thin line). (Upper panel) $\cos\,\theta^-_{45}$.

With range discretization, the coupling effect on acoustic mode coefficients $A_j e^{i\theta_j}$ (phasors) may be written

$$\begin{pmatrix} C_{11} & C_{12} & \cdots & C_{1m} \\ C_{21} & C_{22} & \cdots & C_{2m} \\ \vdots & \vdots & \vdots & \vdots \\ C_{m1} & C_{n2} & \cdots & C_{mm} \end{pmatrix} \begin{pmatrix} A^-_1 e^{i\theta^-_1} \\ A^-_2 e^{i\theta^-_2} \\ \vdots \\ A^-_m e^{i\theta^-_m} \end{pmatrix} = \begin{pmatrix} A^+_1 e^{i\theta^+_1} \\ A^+_2 e^{i\theta^+_2} \\ \vdots \\ A^+_n e^{i\theta^+_n} \end{pmatrix}. \tag{12}$$

Superscript $-$ indicates the source side of the sudden interface, which is termed the input side, and $+$ indicates the receiver (output) side. The receiver-side coefficients are of the form

$$M^+_j = A^+_j e^{i\theta^+_j} = \sum_m C_{jm} A^-_m e^{i\theta^-_m}. \tag{13}$$

This is a coherent sum which depends on the phase of each contributing term. Since the mode wavelengths are only a few meters, slowly varying relative phase terms are useful, obtained by dividing by the phase of a reference mode

$$M^{+r}_j = A^+_j e^{i\theta^+_j} e^{-i\theta^+_r} = \sum_m C_{jm} A^-_m e^{i\theta^-_{mr}} \tag{14}$$

where $\theta^-_{mr} = \theta^-_m - \theta^-_r$ in the limit of infinitesimal spacing in the sudden approximation.

For illustration, consider only two propagating modes. In this situation,

$$M^+_i = C_{ii} A^-_i e^{i\theta^-_i} + C_{ij} A^-_j e^{i\theta^-_j} \tag{15}$$

$$M^+_j = C_{ji} A^-_i e^{i\theta^-_i} + C_{jj} A^-_j e^{i\theta^-_j}. \tag{16}$$

The relative phase of the two phasors on the right has a crucial effect. If they are in quadrature, then the coupling will cause a phase shift in M^+ relative to the precoupling value. If the phasors are parallel, then the magnitude will change. In some situations the phasing is less critical, for example, the C_{ij} term can be neglected for the case of weak coupling and unequal mode energies $A^-_i \gg A^-_j$. The simple pair-wise analysis fails in the more general case of many interacting modes, which is the case with continental-shelf solitary waves.

Figs. 19–21 also show the cosines of the intermode phases θ^-_{mr} for $mr = 41$, 51, and 54. The phases are seen to be strongly altered by coupling in the steep faces of the waves, compared with their predictable oscillatory nature away from the packet. This is consistent with alteration of the phasor sum (13) as modal phases and C_{jm} fluctuate in the steep faces of the solitons. Modes 4 and 5, being the most energetic in the left-hand wave face, behave most like the two-mode example (15) and (16), showing coupling at that point when $|\cos(\theta_{54})| \approx 1$.

Although the phase behavior within the packets differs for the three ranges, the net packet effect can nonetheless be described as in (10). This is consistent with our knowledge that coupling by solitons behaves as coupling by two interfaces [6], so that integrated effects in the gray coupling areas of Figs. 19–21 collapse into phase-screen type effects. The sudden (interface) approximation can be used to write a more detailed analog to the full-packet expression (6), with two couplings ($\mathbf{C}$) per soliton and free-space propagation ($\mathbf{\Lambda}$) between couplings. The additional terms would be factors in the more complex form of (6). The propagation and coupling terms would be stable with respect to the packet position, and just as with (6) and (11), only the mode phase terms would be sensitive to packet position. Consistent with this, the previous section has shown that phasing of modes at the source side of the packet directly determines the output modal structure, so that interactions in the interior must also follow a pattern determined by the input phasing. The linear nature of the mode-coupling process (13) prevents the net coupling effect of a translating packet of fixed shape from behaving chaotically or randomly.

VII. Temporal Coherence

Moving-packet intensity (Fig. 10) and energy (Fig. 9) fluctuations exhibit characteristic scales. Fluctuations with respect to R_p can be changed to the temporal domain by dividing by packet speed. The temporal behavior is described using lagged autocovariances of log-intensity and E_m. The autocovariance of E_m is strongly dependent on the general location of a moving packet (either near-source or near-receiver), whereas the autocovariance of log-intensity is not.

The autocovariance of log-intensity at depth z is defined as $C_i(\tau, z) = \langle I_m(t, z) I_m(t+\tau, z)\rangle$, with log-intensity defined as $I_m(t, z) = 10\log_{10}(p^2(t, z)/\overline{p}^2(z))$. The overline indicates average over the simulation. $I_m(t, 45)$ from simulations A, C, and D are plotted in Fig. 22. The conversion from R_p to time assumes a packet speed of -0.8 m/s (toward the source), slightly faster than the linear mode-1 phase speed and comparable to speeds observed in SWARM [7].

$C_i(\tau, 45)$ from these time series, limited to the results with the packet within 8 km of the source, are plotted in Fig. 23. There is no packet for the background-only simulation D, but graphs are aligned such that the results of simulations C and D at a given time result from identical quasi-random thermocline perturbation fields. The results shown use signals from roughly

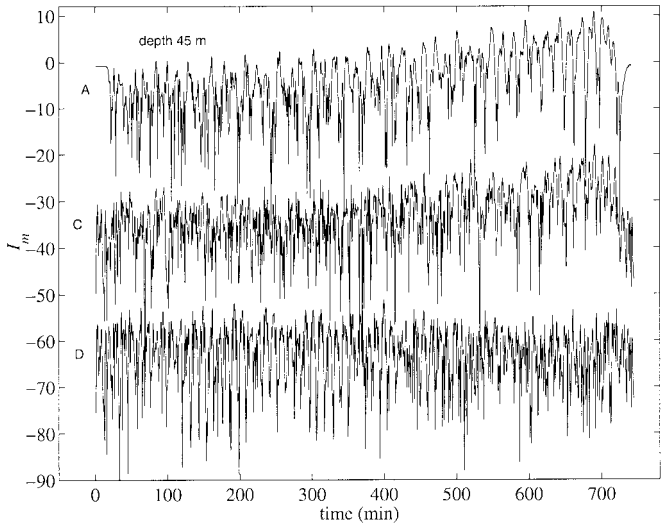

Fig. 22. The modeled log-intensity I_m is plotted at 45-m depth for three simulations. The top is from simulation A, with a moving packet composed of 10-, 12-, and 15-m tall waves. The next trace is from simulation C, with the same packet moving in a background of quasi-random thermocline displacement, offset 30 dB down. The lowest trace is from simulation D, with only quasi-random displacements (identical to those of C), offset 60 dB down. Packet near the receiver (high R_p) is at the left and packet near the source (low R_p) is at the right.

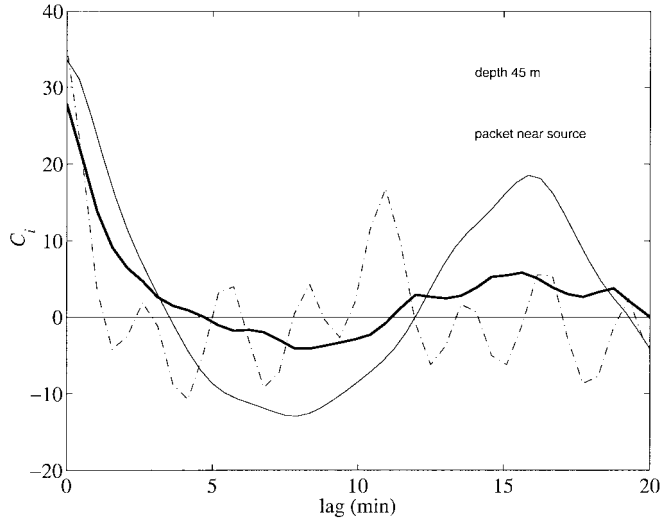

Fig. 23. Temporal autocovariance functions for 45-m signals with the soliton packet within 8 km of the source. These signals are on the right-hand side of Fig. 22. Shown are: simulation A, packet only (thin line); simulation C, packet and background displacements (thick line); and simulation D, only the background of simulation C (dash–dotted line).

the right-hand 170 min of Fig. 22. Likewise, C_i from these time series with the packet within 8 km (170 min) of the receiver are plotted in Fig. 24 (signal from the left-hand side of Fig. 22). The decorrelation time is about two minutes for both sets of packet-only fluctuations (simulation A), possibly a little bit longer with the packet near the source, with variance of about 33 dB^2. There is a significant correlation at 16 min lag with the packet near the source, showing structure in the fluctuations. The decorrelation times with packets moving through a background field (simulation C) are also about two minutes. The simulation C results for the near-source and near-receiver packet situations are even more similar to

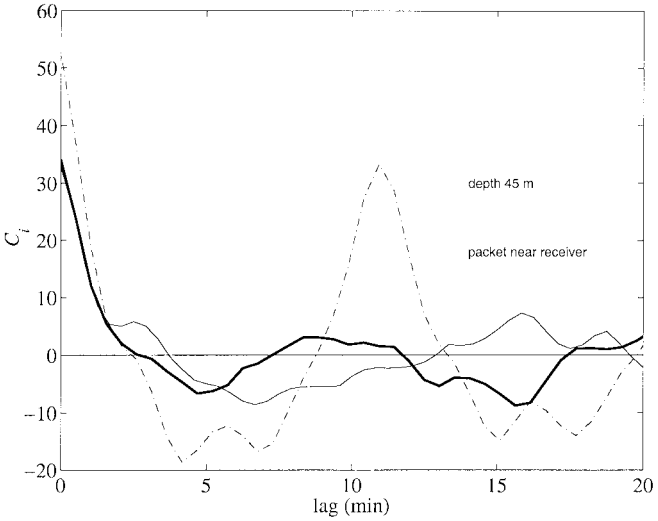

Fig. 24. Temporal autocovariance functions for 45-m signals with the soliton packet within 8 km of the receiver. These are the left-hand third of the signals in Fig. 22. The line types are as in Fig. 23.

each other than the simulation A results. The autocovariance computed for propagation through the quasi-random wavefield (simulation D, dash–dotted lines) shows sensitivity over time of decorrelation time and of variance level, evident as a difference of the dash–dotted lines in the figures, an artifact of using only one realization of the quasi-random field. The true autocovariance for wavefields of this type can only be estimated from the figures.

Results for other depths show similar 2-min decorrelation times but have different variances. Overall, C_i at all depths have consistent forms, similar to those shown, for any conditions with a packet moving in a zone between the source and the receiver, regardless of packet proximity to source or receiver and regardless of the presence of background thermocline displacement.

The autocovariance of the signal energy E_m is similarly defined, $C_E(\tau) = \langle E_m(t)E_m(t+\tau)\rangle$. $C_E(\tau)$ are shown for simulations A, C, and D with packet locations either near the source or receiver (Figs. 25 and 26), analogous to the C_i presentation. Unlike C_i, C_E shows strong variation. A packet moving near the source gives a variance of 8 dB^2, with or without additional quasi-random thermocline displacements, with a decorrelation time of 3 or 4 min. A packet moving near the receiver without additional quasi-random displacements is remarkably different, giving essentially no signal variability, a fraction of a decibel. A packet moving near the receiver in quasi-random fluctuations (simulation C) gives variance of about a decibel and has temporal coherence very similar with that of background fluctuations alone (simulation D). The effect of quasi-random fluctuations throughout the medium swamps the effect of a packet near the receiver, largely through the action of fluctuations near the source alternately transferring energy into or out of mode 1, comparable to packet effects described in Sections V and VI. The effect of a packet near the source swamps the random wavefield effect.

The C_E autocovariances show decorrelation times of 3 to 4 min for both random fluctuations and packets, despite

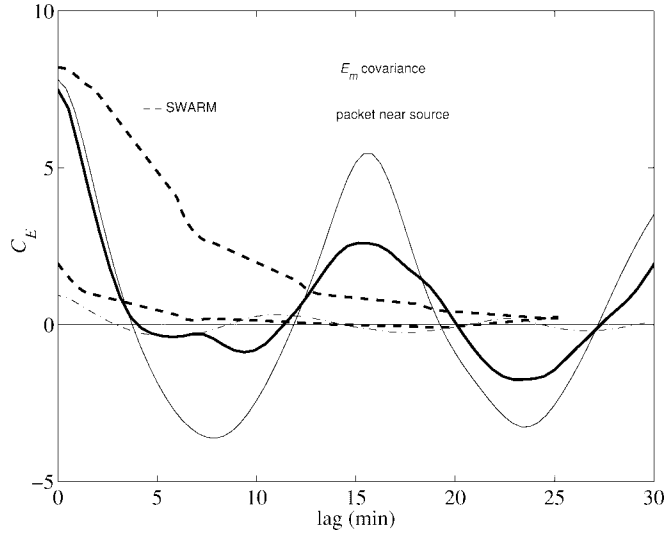

Fig. 25. Temporal autocovariance functions of E_m with the soliton packet within 8 km of the source. Shown are: simulation A, packet only, see Fig. 8 (thin lines); simulation C, packet and background displacements, see Fig. 14 (thick lines); and simulation D, background only from simulation C, see Fig. 13 (dash–dotted line). The thick dashed lines show covariance functions for two 1-h sections of the SWARM data (Fig. 2).

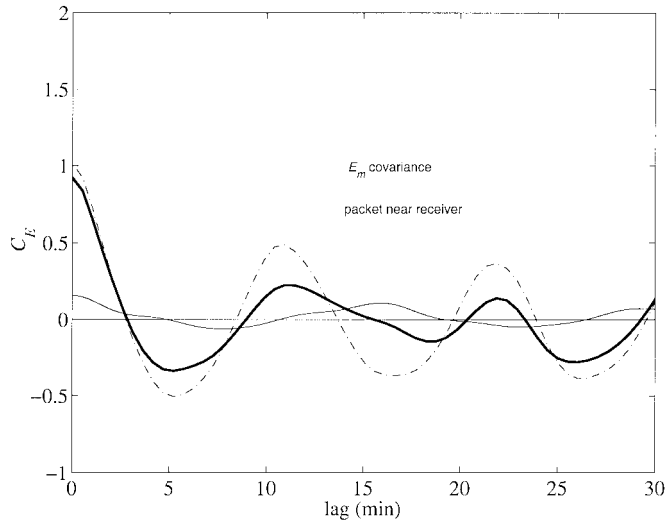

Fig. 26. Temporal autocovariance functions of E_m, as in Fig. 25, except with the packet within 8 km of the receiver. The line types are as in Fig. 25. The covariances from the wave packet cases (thick and thin lines) are weak compared to those with the packet near the source (Fig. 25).

the strong differences in variance for packets and random fluctuations. This time scale corresponds to packet movements of about 150 m for a packet speed of 0.8 m/s. These results can be compared with autocovariances of SWARM log-energy I (Figs. 2 and 25). Autocovariances from two 1-h SWARM periods are shown, the second and the eleventh hour of Fig. 2(a). The hour 2 signals show about 8-dB^2 variance and about a 9-min time scale. The hour 11 signals show a 2-dB^2 variance and about a 5-min time scale. These depth-averaged SWARM pulse fluctuations (energy fluctuations) have slightly longer coherence time scales than our simulations and have comparable variances. We have no simple explanation for the discrepancy.

VIII. Smoothing of Mode Energy Content

Section V showed that acoustic energy fluctuations at distances of many kilometers beyond a packet are determined by flux into or out of low modes which propagate well, 1 and 2. If mode-1 energy were strong before encountering a packet, one would expect signal loss on average via coupling to high modes. If higher mode energy were to exceed mode-1 energy before packet encounter, then one would expect gain. The second scenario occurred in simulation A.

One generalization of this behavior would be a process of energy smoothing between modes. This would occur if packet-induced coupling had no preferred direction in mode space. It is unclear from our simulations whether such nondirectionality is a good assumption. If the couplings at each face of each soliton in a packet were truly random and symmetric, then the transfer of energy from energized (noisy) modes to quiet modes might be analogous to diffusion in mode space. The situations in this paper, with three large waves of fixed shape, are more orderly and are directly controlled by modal phase cycling, shown by the near-periodicity in Fig. 9. Nonetheless, stretching the diffusion analogy, the hypothesis that packets transfer energy from energetic (noisy) to quiet modes is investigated here using simulation output.

Varying the source depth will change the relative excitation levels of the modes. Excitation is efficient for modes peaking at the source depth and inefficient for those with nulls at the source depth. Mode 1 is weak near the surface and will only be strongly excited only by deep sources. We compute mode excitation by a source at depth z_s using [19]

$$M_j(0) = i\pi\Psi_j(z_s)\left(\int_{-\infty}^{0}\Psi_j^2(z)\,dz\right)^{-1}. \qquad (17)$$

Fig. 27 shows the excitation of the first nine modes for three source depths, 18, 32, and 44 m. Mode-1 excitation is weak for the 18-m source compared with the others, as expected, and modes 2 and 6 are also weakly driven. The 32-m source shows weak excitation of mode 7. The 44-m source shows a slight weakness at mode 2 and weakly drives mode 5.

Depth-integrated energies at 33-km range resulting from propagation through moving packets for the three source depths are shown in Fig. 28. The results for 18-m source depth (simulation A) indicate amplification with the packet near the source (a focus of earlier sections) but the the other results do not. We wish to determine whether comparison of mode 1 and higher order mode excitation levels allows prediction of the level of gain introduced by the packet. Higher order mode excitation will be expressed here as the incoherent sum of mode 2–5 amplitudes at the source, summed over the water column to be more comparable with E_m. The excitation measure is $\Delta X_{2:\,5,\,1} = 10\log_{10}(\int dz \sum_{n=2}^{5}|F_n|^2/\int dz|F_1|^2)$, where F_n is the acoustic field associated with mode n.

Fig. 29 compares signal gain and $\Delta X_{2:\,5,\,1}$. Two gain measures are plotted: peak gain relative to the no-soliton case obtained from 33-km output such as in Fig. 8, and peak gain obtained from smoothed forms of the 33-km output. The smoothing process is a 3200-m triangle filter (toe to toe),

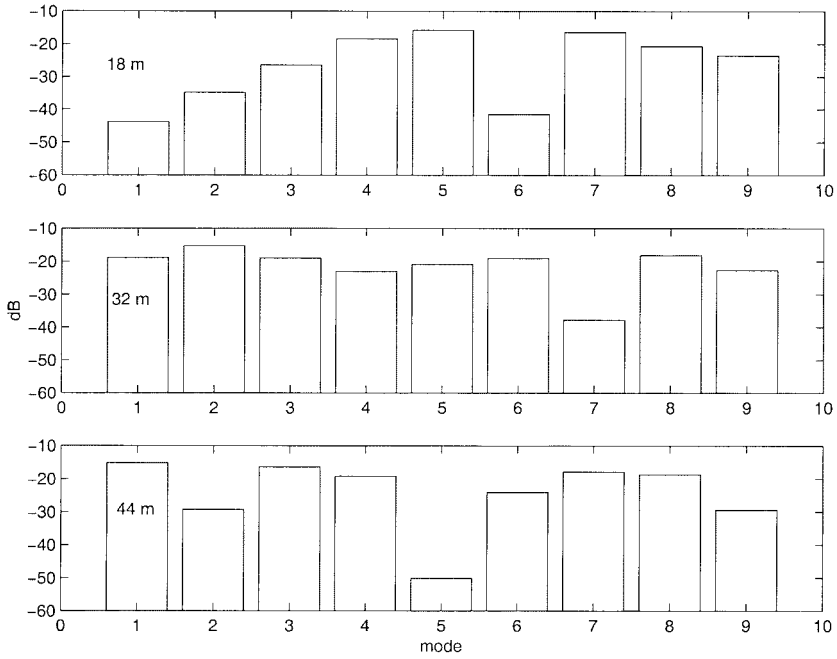

Fig. 27. Excitation levels for the first few modes at three source depths: 18, 32, and 44 m.

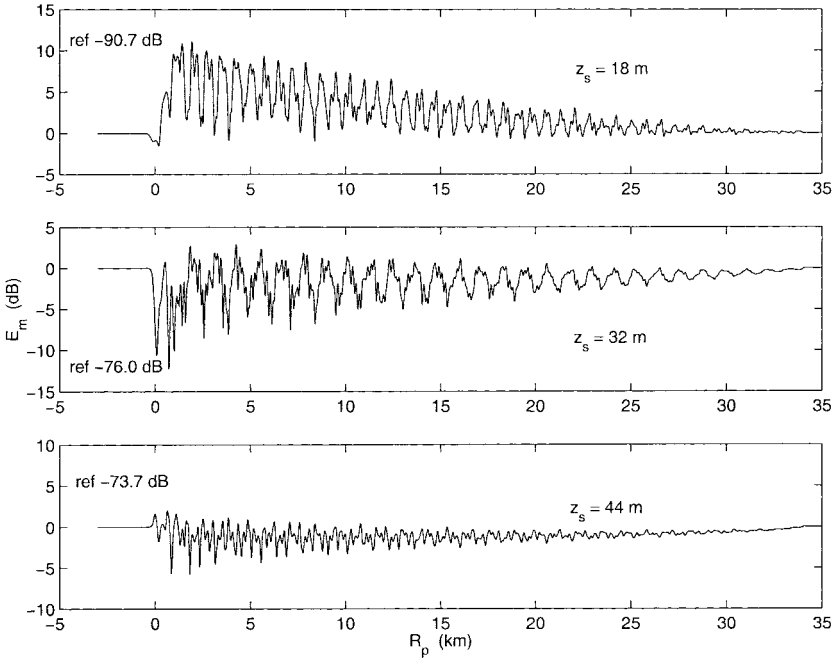

Fig. 28. E_m versus R_p for three source depths.

intended to dampen the effects of the fluctuations examined in the three previous sections.

The figure shows one-to-one correlation between gain and strength of mode 2–5 excitation. That is to say, each case with greater energy in modes 2–5 than in mode 1 exhibited gain greater than unity, and each case with less energy in modes 2–5 than in mode 1 exhibited gain less than unity. Gain versus relative excitation does not fall on a smooth curve, but the tendency is always for excitation of modes 2–5 (relative to mode 1) and gain to go together. Thus, signal gain is in an average sense a function of the ratio of high-mode energy to mode-1 energy. A more precise study of mode-coupling tendencies would include analysis of mode levels just before and just after packets. This tendency for the mode energies to be equilibrated by coupling does not hold instantaneously because of the strong fluctuating coupling responses to mode phase cycling. More detailed analysis of gain behavior for this particular soliton packet moving in this particular acoustic (and hydrodynamic) waveguide is not warranted if one considers that uncountable other waveguides are possible and reasonable. However, the physical effect illustrated here should hold for any situation of a packet moving in a waveguide.

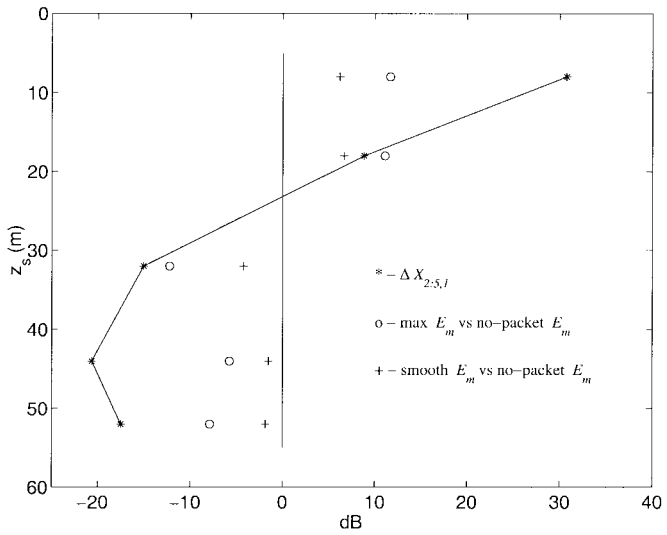

Fig. 29. Incoherent excitation of modes 2–5 is compared to mode-1 excitation for five source depths z_s (line). For the same five source depths, maximum observed with-packet E_m (o) and smoothed E_m (+), relative to no-packet E_m, are also plotted. The vertical line indicates no gain, and all situations with excess excitation in high modes ($\Delta X > 0$ dB) show gain from the packet, while situations with a high-mode excitation deficit show loss.

IX. Summary

Simulations show that 400-Hz sound propagating through a moving packet of coastal internal solitary waves in 50-m-deep water will have strong energy fluctuations in the case of near-adiabatic propagation for tens of kilometers after the packet. The fluctuations are caused by mode coupling at each face of each solitary wave in the packet. In addition to the fluctuations, signal energy averaged over periods of order one hour exhibit amplification (or loss) if the packet is near the source. This gain process is linked to the modal content of the source signal and occurs via transfer into (or out of) the efficiently propagating low-order modes from (or to) the more lossy high-order modes. Gain occurs if high-order modes are excited by the source and coupling is to low-order modes; loss occurs if the opposite is true.

Although we have considered only one packet geometry and one acoustic waveguide, we have demonstrated some links between the packet characteristics and the signal strengths measured at a distant vertical line array. Some of the characteristics of the fluctuations are understandable and may be predictable in detail with a basic knowledge of the stratification and the wave shapes. For example, the coupling of modes by a translating packet of fixed shape can accurately be described by a fixed coupling matrix operation. This means that the phases of the modes which are operated on by the matrix (packet) are the most rapidly changing variables in the problem and govern the fluctuation time scales. This is probably also true for the slowly varying packet case (not examined). Analysis shows the further result that coupling behavior can be governed by interference patterns between modes which each couple strongly to an output mode. The situation examined here, with our chosen packet shape and acoustic waveguide, shows variable net coupling to mode 1 by the packet, which gives signal energy variability at a distance. The fluctuating coupling is directly associated with interference of modes 4 and 5.

Specific results demonstrate the importance of the effects. A source at 18-m depth weakly excites mode 1 in our model waveguide, and in this situation fluctuations of depth-averaged energy due to coupling by packets with wave amplitudes of 10 to 15 m are of order 10 dB. This is about five times the magnitude of energy fluctuations arising from smaller amplitude background thermocline displacements filling the region. The 18-m source situation gives a peak of 11 dB of gain if the packet is near the source, with 7-dB average gain. A source at 44-m depth, exciting mode 1 more efficiently than the 18-m source, gives a peak loss of 6 dB and an average loss of 2 dB.

Intensity fluctuation time series measured at a fixed depth are comparable for the two cases of propagation through moving packets and through a quasi-random thermocline displacement field. The series have similar variances and decorrelation times. Each situation has fluctuations in modal energy and modal phase which complicate the fixed-depth arrivals. The mode couplings by packets (range-restricted and powerful) and the random-field mode couplings (spatially distributed but weak) have different effects on modal content at distant range, but this does not show up in the fixed-depth acoustic records. The difference does show up in the signal energy, measured with a vertical line array.

Much of the paper has been devoted to analysis of mode phasing and its effect on packet coupling. The fluctuations, which have been averaged to get the mean results stated above, are caused by changing phase relationships between modes at the packet as the packet moves. This is intuitive for the unchanging moving packets we consider since phase is the only parameter which changes rapidly. The concept of interacting dominant modes controlling modal changes by entire packets has emerged, similar to a dominant mode paradigm for single-soliton coupling [6].

This study has been limited to the case of a translating packet of symmetric solitary waves with fixed geometric shape in a homogeneous waveguide. This study has not considered possibly complicating or competing effects of heterogeneous seafloor structure, variable depth, stratification changes on scales larger than the packet, nonsymmetric (borelike) character of the waves, and fronts near the wave packet. These can all give fluctuations which can interfere with or mask fluctuations generated by mode coupling at packets. Since so little of the energy is resident in the sea floor, we anticipate that bottom structure will have a weaker direct effect than packets on coupling, but may influence mode phases, coupling at packets, and long-range propagation effects.

Acknowledgment

The SWARM data were generously provided by J. Lynch, A. Newhall, B. Sperry, and B. Headrick.

References

[1] J. M. Huthnance, "Internal tides and waves near the continental shelf edge," *Geophys. Astrophys. Fluid Dynamics*, vol. 48, pp. 81–106, 1989.

[2] J. R. Apel, L. A. Ostrovsky, and Y. A. Stepanyants, "Internal solitons in the ocean," The Johns Hopkins Univ. Applied Physics Lab., Laurel, MD, Rep. MERCJRA0695, 1995.
[3] J. Zhou, X. Zhang, and P. H. Rogers, "Resonant interaction of sound wave with internal solitons in the coastal zone," *J. Acoust. Soc. Amer.*, vol. 90, pp. 2042–2054, 1991.
[4] J. Zhou, X. Zhang, P. H. Rogers, D. Wang, and E. Luo, "Anomalous sound propagation in shallow water due to internal wave solitons," in *Proc. Oceans'93*, New York, NY, 1993, vol 1, pp. 87–92.
[5] M. K. Broadhead and H. B. Ali, "Dissipative shallow water internal waves and their acoustical properties," in *MTS/IEEE Oceans'95: Challenges of Our Changing Global Environment*, New York, 1995, vol. 1, pp. 673–684.
[6] J. C. Preisig and T. F. Duda, "Coupled acoustic mode propagation through continental-shelf internal solitary waves," *IEEE J. Oceanic Eng.*, vol. 22, pp. 256–269, 1997.
[7] J. R. Apel, M. Badiey, C.-S. Chiu, S. Finette, R. Headrick, J. Kemp, J. F. Lynch, A. Newhall, M. H. Orr, B. H. Pasewark, D. Tielbuerger, A. Turgut, K. von der Heydt, and S. Wolf, "An overview of the 1995 SWARM shallow water internal wave acoustic scattering experiment," *IEEE J. Oceanic Eng.*, vol. 22, pp. 465–500, 1997.
[8] R. H. Headrick, "Analysis of internal wave induced mode coupling effects on the 1995 SWARM experiment acoustic transmissions," Ph.D. dissertation, MIT/Woods Hole Oceanogr. Inst. Joint Program, 1997.
[9] R. H. Headrick, J. F. Lynch, J. R. Apel, M. Badiey, C.-S. Chiu, S. Finette, J. Kemp, A. Newhall, M. H. Orr, B. H. Pasewark, D. Tielbuerger, A. Turgut, K. von der Heydt, and S. Wolf, "Acoustic normal mode fluctuation statistics in the 1995 SWARM internal wave scattering experiment," *J. Acoust. Soc. Amer.*, submitted for publication.
[10] H. Sandstrom and N. S. Oakey, "Dissipation in internal tides and solitary waves," *J. Phys. Oceanogr.*, vol. 25, pp. 604–614, 1995.
[11] L.-L. Fu and B. Holt, "Internal waves in the Gulf of California: Observations from a spaceborne radar," *J. Geophys. Res.*, vol. 89, pp. 2053–2060, 1984.
[12] A. K. Liu, "Analysis of nonlinear internal waves in the New York bight," *J. Geophys. Res.*, vol. 93, pp. 12,317–12,329, 1988.
[13] P. F. Worcester, R. C. Spindel, and B. M. Howe, "Reciprocal acoustic transmissions: Instrumentation for mesoscale monitoring of ocean currents," *IEEE J. Oceanic Eng.*, vol. OE-10, pp. 123–137, 1985.
[14] M. D. Collins, "FEPE user's guide," Naval Ocean Research and Development Activity (NRL-SSC), NORDA Tech. Note 365, Stennis Space Center, MS, 1988.
[15] M. D. Collins and E. K. Westwood, "A higher-order energy-conserving parabolic equation for range-dependent ocean depth, sound speed, and density," *J. Acoust. Soc. Amer.*, vol. 89, pp. 1068–1075, 1991.
[16] D. Tielburger, S. Finette, and S. Wolf, "Acoustic propagation through the internal wave field in a shallow water waveguide," *J. Acoust. Soc. Amer.*, vol. 101, pp. 789–808, 1997.
[17] O. A. Gilman, R. Grimshaw, and Y. A. Stapanyants, "Dynamics of internal solitary waves in a rotating fluid," *Dyn. Atmos. Oceans*, vol. 23, pp. 403–411, 1996.
[18] A. D. Pierce, "Extension of the method of normal modes to sound propagation in an almost-stratified medium," *J. Acoust. Soc. Amer.*, vol. 37, pp. 19–27, 1965.
[19] L. M. Brekhovskikh and Y. P. Lysanov, *Fundamentals of Ocean Acoustics*. New York: Springer-Verlag, 1991.

Timothy F. Duda received the B.A. degree in physics from Pomona College, Claremont, CA, in 1979 and the Ph.D. degree in oceanography from Scripps Institution of Oceanography, University of California at San Diego in 1986.

He has been a Scientist at the Woods Hole Oceanographic Institution, Woods Hole, MA, since 1991, and prior to that he was a Research Scientist at the University of California, Santa Cruz. His two primary fields of study are the measurement and characterization of ocean internal waves and microstructure, and ocean acoustic propagation. He has modeled and analyzed fluctuations of ocean acoustic transmissions, has made electromagnetic-type internal wave measurements, and performed *in situ* measurements of ocean microstructure.

Dr. Duda is a member of the American Meteorological Society, the American Geophysical Union, and the Acoustical Society of America.

James C. Preisig (S'87–M'91) received the B.S. degree in electrical engineering from the U.S. Coast Guard Academy in 1980, the S.M. and E.E. degrees in electrical engineering from the Massachusetts Institute of Technology (MIT), Cambridge, MA, in 1988, and the Ph.D. degree in electrical and ocean engineering from the MIT/Woods Hole Oceanographic Institution (WHOI) Joint Program in Oceanography and Oceanographic Engineering, Woods Hole, MA, in 1992.

Prior to joining WHOI as a Scientist, he was a Visiting Assistant Professor in the Department of Electrical and Computer Engineering at Northeastern University, Boston, MA, and a Visiting Investigator at WHOI. His research skills are in adaptive signal processing, signal propagation modeling, and numerical optimization. He currently applies these skills in three research programs. The first is the development of a better understanding of the effect which environmental fluctuations have on propagation acoustic and electromagnetic signals, the second is to use this understanding to develop adaptive signal processing algorithms with improved performance characteristics, and the third area is the development of computationally robust and numerically efficient techniques for implementing new adaptive algorithms.

Dr. Preisig is a member of the Sensor Array Processing Technical Committee